ASTRONOMY & ASTROPHYSICS
SUPPLEMENT SERIES

Astron. Astrophys. Suppl. Ser. **136**, 245–256 (1999)

Dust continuum imaging of C/1995 O1 (Hale-Bopp):

Rotation period and dust outflow velocity

J. Warell, C.-I. Lagerkvist, and J.S.V. Lagerros

Astronomiska Observatoriet, Box 515, SE-751 20 Uppsala, Sweden

Received March 12; accepted November 4, 1998

Abstract. Dust continuum imaging of comet C/1995 O1 (Hale-Bopp) was carried out with the Swedish Vacuum Solar Telescope (SVST) on La Palma, Spain, during the period April 21–25, 1997. CCD observations were made with λ 550 nm and λ 830 nm filters, with band-passes excluding major cometary gaseous emissions. Images were reduced according to standard procedure, aligned, averaged, navigated and enhanced with azimuthal renormalisation, rotational and temporal derivative and unsharp masking techniques.

The rotation period of the nucleus was determined to $11\overset{\mathrm{h}}{.}46$ and the mean projected dust outflow velocity to 0.41 km s^{-1} measured over a radius range of 5 000 − 45 000 km. No difference in quasi-simultaneous dust morphology between the filter wavelengths was seen. Up to five shell envelopes were visible in the sun-ward side of the coma out to a radius of 80 000 km, separated by a projected distance of $\sim$15 000 − 20 000 km and spiralling towards smaller radii in the direction of local evening. Outer boundaries of shells were more sharply defined than inner, with shell intensity maxima occurring at $\sim35^\circ$ past the sun-comet line in the direction of rotation. Small scale inhomogeneities of size 1 000 − 2 000 km were seen at radii $\leq$ 20 000 km. Two superposed shell systems with a relative lag angle of $\sim55^\circ$ were evident during the period of observation.

The sense of rotation of dust emission features indicates that the north pole of the nucleus was directed towards the Earth. The shape of the incomplete spiral shell pattern indicates that the angle between the line-of-sight and the rotation axis of the nucleus was not very large.

Key words: comets: individual: c/1995 01 Hale-Bopp — techniques: image processing

Send offprint requests to: Johan.Warell@astro.uu.se

1. Introduction

By analysis of the emission structure on high-resolution dust-continuum images, the rotation period of the nucleus and the mean dust outflow velocity may be determined, and constraints may be set on the direction of the axis of rotation. Numerical simulation experiments and hydrodynamic modelling, based on observed structures in the inner coma, is a means of constraining fundamental properties of the emission properties of the nucleus and its dust and gas emission. One of the goals of such models is the determination of the physical properties and the activity pattern of the nucleus on the basis from observations, such as images of the coma structure.

Some steps have been taken towards reproducing by modelling some observed features in the coma of a number of comets, such as jet-like features of Hale-Bopp (Sekanina 1998; Sekanina & Boehnhardt 1998) and Halley (Crifo 1997b and references therein), but determination of detailed nucleus emission properties from imaging observations is currently not possible. Coma morphology has been modelled for comets in general and as specific objects (e.g., Sekanina & Larson 1986 and references therein; Sekanina 1987) and for Hale-Bopp specifically (e.g., Sekanina & Boehnhardt 1988; Sekanina 1998; Samarasinha et al. 1998). These works do not take into account interaction processes between outflows subsequent to emission from the active areas.

It has become evident that the formation of structures in cometary comae and their relation to nucleus activity is very complex and requires gas-hydrodynamic modelling in order to obtain an understanding of the underlying processes. The results of such models, incorporating outflow interaction processes, have been published for pure gas and dusty-gas emission cases and for surface topography (Kömle & Ip 1987; Kitamura 1986, 1987, 1990; Keller et al. 1994; Crifo 1995, 1997a, b). For improvement of any future modelling of these processes, ground-based imaging data of high

resolution, such as the data set presented here for comet Hale-Bopp, will be of considerable importance.

C/1995 O1 (Hale-Bopp) reached perihelion on 1997 April 1.137 UT at a heliocentric distance of 0.914 AU (Marsden 1997). The geometry during the period of observation was such that the phase angle of $\sim 35^\circ$ made the morning hemisphere of the nucleus unobservable. As the north pole of the nucleus was visible, the region of the sub-solar point and evening terminator of the nucleus was located in the general direction of the Earth.

In this paper, we present very high-resolution images of the near-nucleus coma of Hale-Bopp, and determine the nucleus rotation period and mean outflow velocity of the dust ejecta. The SVST has been used for successful planetary imaging on a number of occasions (e.g., Lindgren 1995; Warell 1996; Orton et al. 1996). Given the high surface brightness and coma detail of Hale-Bopp, it was therefore natural to use the instrument for specific studies of the intricate dust morphology of its inner coma. The apparition of this bright comet made it a unique target for studying the coma morphology close to the nucleus, and the high spatial scale obtainable with the SVST at its excellent site made it a very good instrument for such an investigation.

2. Observations

Observations of comet C/1995 O1 (Hale-Bopp) were carried out with the 0.50 m Swedish Vacuum Solar Telescope (SVST) on La Palma. Images were taken during the period April 21–25, 1997, three weeks past perihelion. At the site, the value of the cometary phase angle made optical observations possible during a period of at most one hour in a gradually darkening twilight sky, while the altitude of the comet decreased from 20° to 7°. Ephemeris data (Yeomans 1997) is given in Table 1.

In its nominal configuration, the SVST operates at focal ratio f/45 and focal length F 22.3 m, measured at λ 550 nm (Scharmer 1985). For increased field coverage, auxiliary compressing optics were installed for an F 7.7 m, f/15, configuration. A Kodak Megaplus 1.6 CCD 10-bit camera with a KAF-1600 chip having $1\,536 \times 1\,024$ imaging pixels of 9×9 micrometer size was used. The camera operated at $0 - 12$ dB gain with no cooling at a stable ambient temperature of 20°C.

Dust continuum imaging was performed with Ealing 550 nm and 830 nm band-pass filters, having FWHM of 43 and 38 nm, and transmission maxima of 80 and 83%, respectively. The steep chromaticity curve of the telescope's achromatic objective prevents useful imaging with filters of wider band-pass than this, while narrow-band filters would imply unrealistically long exposure times for the present target, considering the noise characteristics of the uncooled chip. Exposures were made of a $4\farcm4 \times 6\farcm6$ field centered on the psuedo nucleus, with an image scale of $0\farcs24$ per pixel equalling the diffraction limit of the instrument at λ 520 nm. Exposure times were in the range $1 - 15$ s with photo-centre saturation occurring at the longer exposures. A total of 320 images were obtained, which were subsequently averaged into 37 data images for analysis.

A short description of the optical setup is in order. The converging beam of the system exited horisontally along the surface of a levelled optical table, where auxiliary optics were mounted. Focussing was achieved by moving the table along the direction of the optical axis. The beam was diaphragmed at the first focus to minimize effects of scattered light. A single lens of F 200 mm imaged the first focal plane, and a 70 mm camera objective lens mounted on the CCD head completed the compressive optics setup. The 25 mm diameter imaging filters were positioned in between the lenses.

Contribution of C_2 emission to the total flux from the comet within the λ 550 nm filter passband is estimated to be negligible at a 0.5% level, based on a low-dispersion spectrum by Avila et al. (1997) obtained on April 24[1].

3. Data reduction and processing

For image reduction and processing, the MIDAS software package was used (ESO 1996). Traditional methods were employed for the basic reduction. Master darks, having the same exposure times as the data frames, were made by averaging $20 - 125$ individual frames. Flats in the two filters were taken after sunset during twilights throughout the observing period, and masters were compiled from $15 - 125$ individual frames. Following flat- and dark-correction, individual exposures of the comet were aligned and averaged in sequences of equal exposure times, to increase the signal-to-noise (S/N) ratio. A $S/N \sim 150 - 250$ with respect to the unsaturated photo-centre was achieved for the highest quality images. 37 data frames were thus obtained by averaging for subsequent analysis.

Details of the data set is given in Table 2, where $F(T, z)$ is a relative measure of the flux recorded by the detector in the direction of the comet photo-centre at sky conditions characteristic of the observing period. Its value is given by

$$F(T, z) = T k_\lambda \sec z \tag{1}$$

where T is the total exposure time in seconds and z the zenithal distance of the comet in degrees. The factor $k_{550} = 1$ or $k_{830} = 0.919$ corrects for the respective filter band-passes, total transmissions and CCD quantum efficiency. For a one second exposure towards the zenith through the λ 550 nm filter, the CCD thus records a relative flux level of unity.

[1] At the time of writing, the spectrum may be found on the ESO Hale-Bopp Homepage at http://http.hq.eso.org/comet-hale-bopp/comet-hale-bopp-may15-ga.html

Table 1. Ephemeris data for Hale-Bopp during the observing run. Also given is the equivalent distances of the telescope diffraction limit D at λ 550 nm ($0\farcs28$) and CCD pixel angular size S ($0\farcs24$) at the geocentric distance of the comet. The last two columns give a UT and the position angle of the radius vector (direction to Sun) at that time

Date (0^h UT)		α (J2000.0)	δ	Δ (AU)	r (AU)	Phase	D (km)	S (km)	UT	PA_{Sun}
1997	April 21	$04^h02^m03\fs16$	$+32°32'37\farcs4$	1.602	0.980	$36\fdg7$	325	279	21.5	243.1
	April 22	04 06 32.84	+31 51 57.0	1.619	0.987	36.0	329	282		
	April 23	04 10 53.20	+31 11 30.6	1.635	0.980	35.4	332	285	21.6	246.1
	April 24	04 15 04.71	+30 31 20.9	1.651	1.001	34.7	335	287	21.2	247.5
	April 25	04 19 07.83	+29 51 30.1	1.668	1.008	34.0	339	290	21.2	248.9
	April 26	04 23 02.99	+29 12 00.1	1.685	1.015	33.4	342	293		

Alignment of the images prior to addition was made to 0.1 pixel ($0\farcs03$) accuracy. The alignment was performed with a MIDAS procedure using an intensity weighted first moment of the pixel values within a square aperture to compute the central position of the object. The aperture varied in size between $13-26''$ depending on image brightness. Several overlapping fields containing the approximate photo-centre location were sampled whereby photo-centre positions were obtained. The positions were averaged to determine mean pixel coordinates of the photo-centre. Images with the same exposure time were then added based on these coordinates. After flat- and dark-correction, alignment and addition, the frames were cropped to 512×512 pixel ($123''\times123''$) size symmetric to the photo-centre and remaining cosmetic blemishes were removed by interactive pixel editing and median filtering.

A number of processing methods applicable to comets (Larson & Slaughter 1992) were used to enhance low-visibility details of the innermost coma. Azimuthal renormalisation processing was performed to reduce the average intensity profile around the photo-centre. Pixel intensities of the original image I are here transformed according to

$$I^{\mathrm{ar}}_{r,\theta} = I_{r,\theta} - \frac{1}{n}\sum_{\theta=0}^{2\pi} I(r) \tag{2}$$

where n is the number of pixels within the annulus of radius r. The method was employed by rotating the source frame in steps of $\Delta\theta = 10°$ about the photo-centre location, successively adding rotated frames and normalising the generated image to unity photo-centre intensity. The rotationally normalised image was then subtracted from its source frame.

As the innermost coma was highly asymmetric around the photo-centre, defects were created by this method. This is also true throughout all of the imaged coma, including the prominent shell structure at greater radii, which generated a non-smoothly varying radial intensity profile. This introduced shells of negative intensity in the anti-solar direction at subtraction.

Rotational gradient processing was performed to enhance features due to the rotational component of motion of dust emission. The rotational gradient algorithm performs according to

$$I^{\mathrm{rg}}_{r,\theta} = I_{r,\theta} - I_{r,\theta+\Delta\theta} \tag{3}$$

where $\Delta\theta$ is the amount of rotational shift. $\Delta\theta$ of 10° and 20° were used; at larger values excessive spurious information was introduced, rendering difficulties in interpretation. As the rotational gradient algorithm is a shift difference method, structure in the processed image displays intensity gradients, and thus differences of emission activity. Images may therefore be difficult to interpret in terms of physical opacity within the coma, especially in the case of such an active comet as Hale-Bopp.

Temporal derivative processing was employed to study possible short-term variations in the morphology of the coma. This technique enhances intensity differences between the two involved images due to dust motion, both azimuthal and radial, relative to the photo-centre. Resulting intensity is

$$I^{\mathrm{td}}_{x,y} = I_{t_1,x,y} - I_{t_2,x,y} \tag{4}$$

where t_1 and t_2 are the times of subsequent images. As with the processing methods described above, it is a powerful method of locating moving features but requires great care in interpretation.

Unsharp masking (Gonzales & Woods 1992) processing was used to remove the general radial intensity function of the coma. It is a straightforward method directly depicting locations of features and at the same time removing the major part of the large-scale brightness variations, but not as powerful as the other three methods in the case of an indistinct object. By subtracting a smoothed copy of the original image, having a larger characteristic width and lower mean intensity of the central intensity peak of the source frame, large-scale intensity differences are effectively reduced. The method is applied according to

$$I^{\mathrm{um}}_{x,y} = \mathsf{F}\cdot I_{x,y} \tag{5}$$

where matrix F,

$$\mathsf{F} = \frac{1}{n^2}\mathsf{F}^*_{n,A} \tag{6}$$

is multiplied with each pixel of I. $A \geq 1$ describes the weight w of the high-pass filter F^*, which is a matrix of

Table 2. Observational dataset. N is number of images added for each mean UT, T is total exposure time, z is zenithal distance and F is a measure of the relative recorded flux as described in the text

Mean UT	λ (nm)	N	T (s)	sec z	$F(T,z)$
April 21					
21:15.1	830	5	5	3.80	1.21
21:24.6	830	10	150	4.27	32.28
21:46.5	550	9	135	6.17	21.88
April 23					
21:22.2	550	3	15	4.30	3.49
21:26.8	550	4	32	4.59	6.97
21:29.5	550	16	16	4.79	3.34
21:35.0	550	17	85	5.25	16.19
21:45.4	550	4	80	6.39	12.52
21:50.1	550	2	10	7.06	1.42
21:52.8	550	4	40	7.39	5.32
April 24					
20:34.8	830	10	50	2.60	17.67
20:38.0	830	9	9	2.68	3.09
20:45.5	830	5	75	2.86	24.10
20:50.9	830	15	15	3.02	4.57
21:03.6	830	8	8	3.46	2.12
21:04.2	550	17	17	3.48	4.88
21:04.8	550	9	9	3.50	2.57
21:11.4	550	6	90	3.79	23.75
21:20.6	550	14	70	4.29	16.32
21:25.6	550	8	40	4.61	8.68
21:27.4	550	16	80	4.74	16.88
21:29.1	550	8	40	4.87	8.21
21:39.0	550	5	75	5.78	12.98
21:45.9	550	10	50	6.66	7.51
21:48.2	550	20	100	7.00	14.29
21:50.4	550	10	50	7.38	6.78
April 25					
20:42.9	550	10	50	2.83	17.67
20:49.4	550	9	45	3.01	14.95
20:52.5	550	9	9	3.11	2.89
20:53.7	550	9	9	3.14	2.87
21:03.6	550	7	105	3.51	29.91
21:22.5	830	10	50	4.50	10.21
21:29.4	830	4	60	5.02	10.98
21:33.6	830	5	5	5.39	0.85
21:35.5	830	10	30	5.58	4.94
21:41.5	830	3	45	6.28	6.59

size $n \times n$ where n is an uneven integer. All elements of F^* have numeric values of -1, except for the central element whose value is

$$w = n^2 A - 1. \tag{7}$$

4. Navigation

Due to the alt-azimuthal mounting of the SVST, non-uniform image rotation required navigation prior to measurements of absolute directions. The light sensitivity of the optical setup and imaging system was such that no field stars were recorded in the field of view, thus precluding straightforward calculation of the local coordinate frame based on field star motion and orientation. Unstable tracking of the instrument prevented use of the line of motion of the comet photo-centre across the field for orientation. Absolute navigation was therefore based on measurements of physical features of the planet Mars, which was imaged with the same optical setup.

The relative image rotation of the alt-azimuthal system relative to the equatorial system occurring between two objects located at different positions on the celestial sphere is obtained from spherical trigonometry. After determination of the absolute orientation of the CCD frame pixel system to the equatorial system at one time, the image rotation is resolved, assuming a fixed optical setup. Features on the disk of Mars were used as an absolute orientation reference.

The sky-projected direction of the rotation axis of Mars was calculated from high-quality closely temporally spaced images from April 24 obtained with the λ 550 nm filter at a mean central meridian longitude $\omega = 359.5°$. A valid assumption was that the CCD orientation remained fixed to the optical table throughout the observing period (no adjustments of the components of the optical setup were performed during this time span). As the two points defining the orientation of the disk on the sky, the photo-centre of north polar ice cap and the geometric centre of the illuminated disk were chosen.

It was assumed that the Martian north polar cap, whose perimeter was wholly inside the visible disk at the observations, was centrally positioned on the geographic pole to the order of the resolution of the data set. The validity of this assumption is confirmed by images obtained by the Hubble Space Telescope WFPC2 in March 1997 (James et al. 1997). At the central meridian of the navigational images of Mars, cap outliers were on the extreme disk edge and did not interfere with the determination of the centre of the main cap deposit. The centre of the main cap was estimated, from HST images, to be located at $0 \pm 15°$ W, $88 \pm 1°$ N. The error estimates equals an apparent angle of $0\farcs05$ from an Earth-based perspective, or a factor five smaller than the pixel angular size. The error in the position of the centre of the cap was determined from the navigational set to $0\farcs09$ or 0.4 pixel.

The centre of the illuminated disk was calculated from isophote contours along the limb, at intensity levels lower than those of the non-geometric limb defects caused by disk albedo variegation. The coordinates of isophote contours were measured to within a fraction of 0.002 of the disk diameter, corresponding to a $0\farcs03$ or 0.1 pixel position error.

Correction was then applied for the phase defect by the position angle and size of the maximum defect of illumination, to yield the centre of the geometric disk. In this

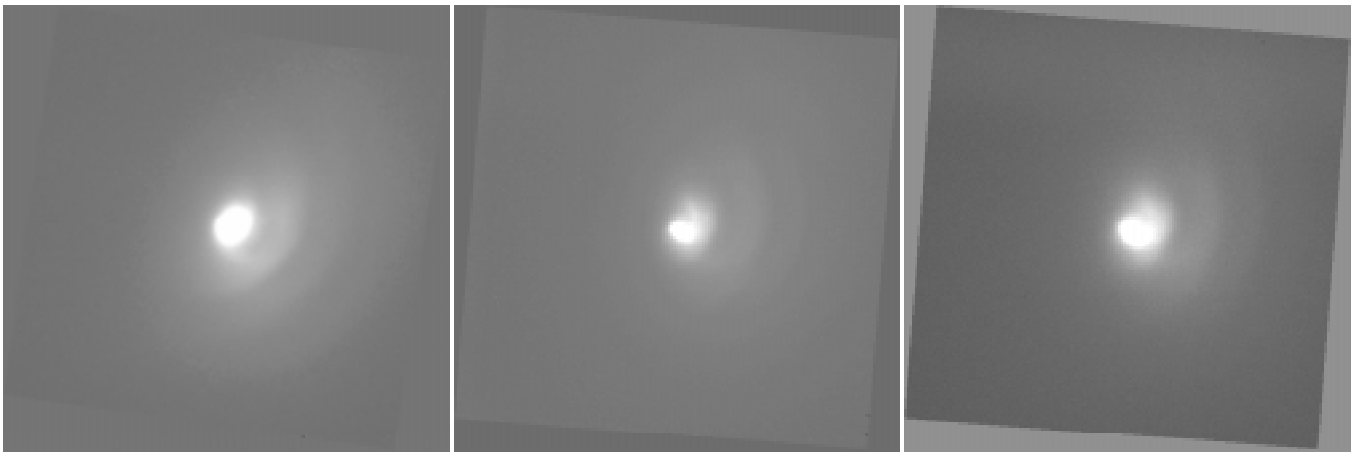

Fig. 1. Examples of navigated images from (left to right) April 21 (21:24.6 UT, filter λ 830 nm), 24 (20:45.5 UT, λ 830 nm) and 25 (20:42.9 UT, λ 550 nm). The April 24 image is the result of adding five images (see Table 2), where the central region of the coma in each image was deliberately saturated at exposure in order to register outer coma structure. Images are flat- and dark-corrected and cleaned by interactive pixel editing, and displayed deliberately saturated near the photo-centre to increase contrast in the fainter coma and shells. A linear gray-scale colour table has been applied. The image field size is 512×512 pixels ($123'' \times 123''$) or 146 000 km at the geocentric distance of the comet, centered on the photo-centre. South is up, west is to the right

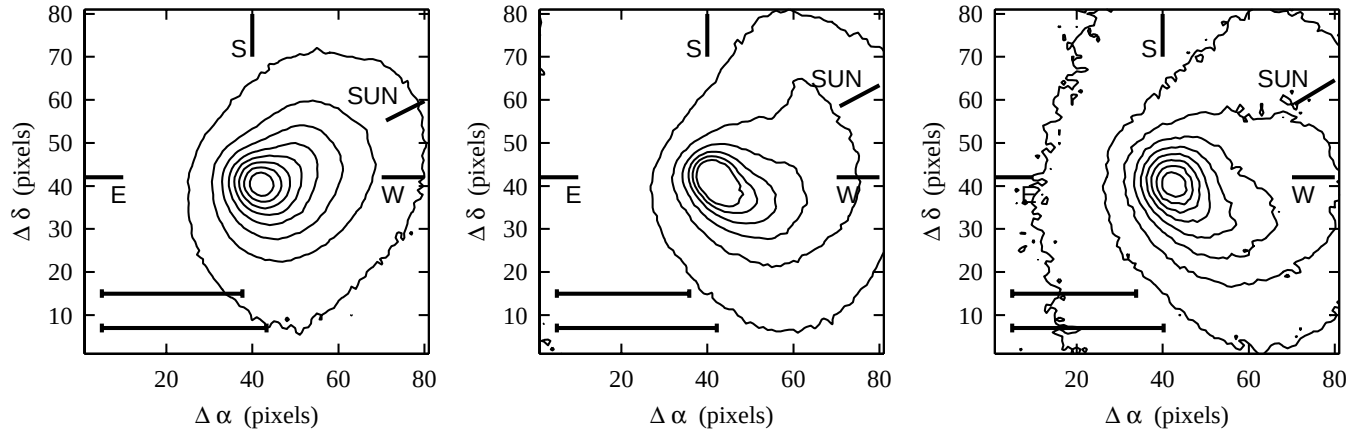

Fig. 2. Isophote contours in 81×81 pixel ($19'' \times 19''$) fields, cropped from the images displayed in Fig. 1 (from left to right, April 21, 24 and 25), and aligned on the calculated photo-centre. Signal-to-noise (S/N) ratios are, respectively, ∼250, ∼260 and ∼90 with respect to the brightness of the photo-centre. Pixel intensity scale is linear and normalised to the interval [0, 1]. Isophote contours are drawn at intensity levels of 0.9, 0.8, 0.7, ... Cardinal points and the direction to the Sun are given. The upper scale bar indicates a spatial distance of 10 000 km at the geocentric distance of Hale-Bopp, the lower bar an angular distance of $10''$. The field size is 28 000 km. The abscissa and ordinate show relative pixel coordinates in the equatorial system (1 pixel = $0.24''$)

step, a tabulated value (Blumberg & Boksenberg 1996) was used for the size of the defect of illumination in combination with the calculated pixel scale and its position angle taken from the images, obtained from the position angle of the line through the cap and illuminated disk centre. The maximum error in the directional angle of the axis of rotation of Mars is, from the above figures, 1.0°.

Thus two points on the disk defining the Martian axis of rotation were known, establishing the orientation of the CCD frame. This measurement was then used to navigate all comet images by the amount of relative image rotation between the times of Mars and comet exposures. In Fig. 1, navigated images of Hale-Bopp reduced with flat- and dark-frame only are shown for three dates during the observing period.

5. Rotation period of the nucleus

The period of rotation P of the nucleus was determined from position angles θ of the maximum elongations of near-nucleus isophotes. Selected images subject only to basic reduction and with the highest S/N were used. The inner isophotes of three April 21, 24 and 25 images are shown in Fig. 2.

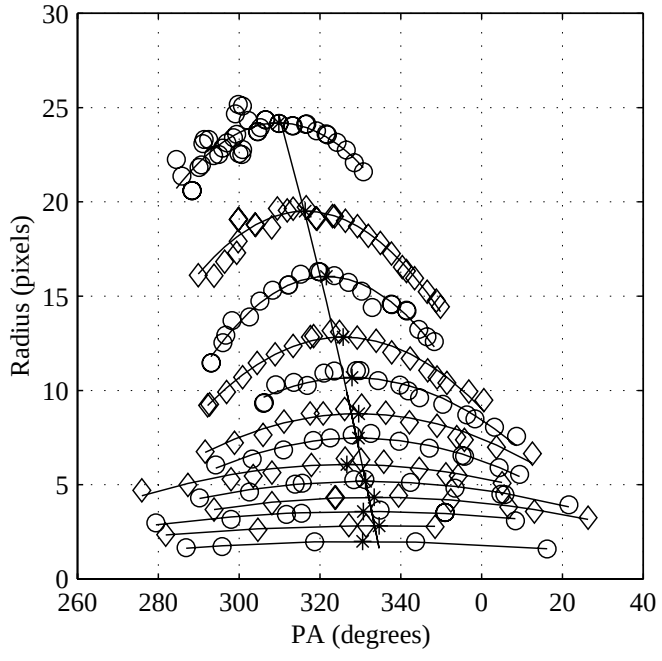

Fig. 3. Fitted isophote data for a number of coma intensity values, for an image obtained April 24 at 21:20.6 UT with a λ 550 nm filter. Each isophote data set has been fitted with a second order curve segment, whose extreme point defines the maximum elongation, i.e. the radius and position angle of the point most distant from the photo-centre, of the particular isophote. The obtained extreme points of the data sets are indicated by asterisks. The extreme points have been fitted with another second order curve (nearly vertical), defining the ($r_{\max}$, θ)-profile, giving the position angle of the near-nucleus elongation as a function of distance from the photo-centre. Ordinate scale is in pixels (1 pixel = 0.24″)

The method consisted of identification of ($r_{\max}$, θ)-coordinates. These defined the radius ($r_{\max}$) and position angle (PA) of the maximum distance from the photo-centre of a specific isophote. The isophote intensities were selected relative to the brightest pixel near the photo-centre. The data points of a segment of each generated isophote centered on the point of maximum elongation was then fitted by least squares with a parabolic segment, whose extreme point defined ($r_{\max}$, θ) of the isophote data subset. Up to 13 isophotes per image were calculated, from which a fraction of 0.2 of the data points were generally selected for the fit. The extreme points obtained from isophote fitting were then used to produce a mean ($r_{\max}$, θ)-profile, displaying the PA of the near-nucleus elongation as a function of distance from the photo-centre (Fig. 3) for the measured range of radii. This method was applied to each image.

Based on images obtained within single nights, times of exposures and shapes of profiles allowed a first determination of the rotational profile $P(r)$. The errors were largest at the inner and outer range of radii, due to the near-circularity of isophotes close to the photo-centre, and the smaller number of images with sufficient S/N at large radii. Combining single-night data from April 23 and 24 yielded a mean nucleus rotation period $P = 11\overset{\text{h}}{.}3 \pm 2\overset{\text{h}}{.}7$ over a range of radii $r = 600 - 9\,600$ km from the photo-centre. The error bounds is for a 50% confidence level, as in the case of all the errors quoted in this work.

The error was reduced by assuming that the same filament, or jet complex, responsible for the major isophote elongation was stable and active throughout the full observing period. Taking into account the ($r_{\max}$, θ)-profile data from all available nights, an improved $P(r)$ was calculated, yielding a nucleus rotation period of $P = 11\overset{\text{h}}{.}46 \pm 0\overset{\text{h}}{.}25$. This value is based on calculating the rotation period at zero radius, based on profiles which were fitted for radii $r = 800 - 9\,300$ km, as described above. The available data points and rotation periods derived are shown in Fig. 5 for a number of radii.

The rotation of the nucleus was in the clockwise sense, thus the north pole of the nucleus was directed towards the Earth.

6. Terminal dust outflow velocity

The projected outflow velocity of the dust emission was estimated from the radial distances of shell trajectories from the photo-centre. From each high S/N image, subjected to basic reduction only, 45 radial profiles at $\Delta\theta = 5°$ angular separations were subtracted by the averaged radial profile extracted from the corresponding azimuthally renormalised image. The range of θ values included the complete span of measurable shell position angles. The profiles thus extracted ideally contains only signal from light scattered and reflected from dust in the shells, and the radial "continuum" should be close to zero. This was true for all radii but those closest to the elongated photo-centre, where the subtraction was incomplete or excessive, depending on the position angle relative to the direction of the major axis of isophote elongation.

The locations of maximum shell intensities for each θ were identified, and the mean radius of each shell, over the available range of position angles, was calculated. A projected radial velocity was obtained from a least squares linear fit of positions versus time. An error estimate was obtained from the radial scatter of data points. Extracted radial intensity profiles and shell positions obtained from an April 21 image is shown in Fig. 4.

An initial estimate on the outflow velocity was obtained from temporal derivative processing of navigated single-night images, from the multi-pixel relative motion of a well-defined edge of an inner shell filament. April 24 images, obtained at the best seeing conditions, showed a spatial movement of ∼4 pixels during a $0\overset{\text{h}}{.}48$ interval, due to rotational and expansional motion of the dust. Based on the expected amount of shell motion resulting from the $\dot{\theta} = 31\overset{\circ}{.}4\ h^{-1}$ rotational angular velocity at the nuclear

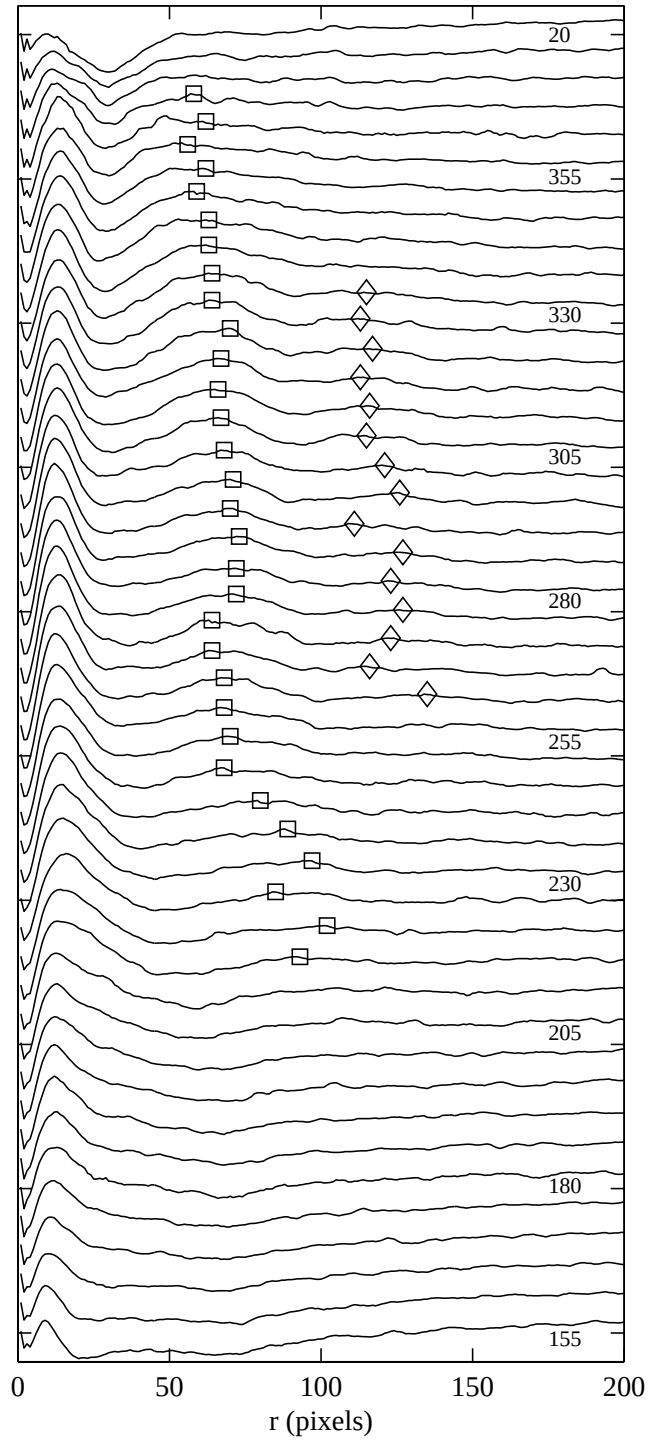

Fig. 4. Radial intensity profiles extracted at 5 degree intervals in PA from an image obtained on April 21 at 21:24.6 UT, subsequent to subtraction by the azimuthally averaged intensity profile. The image is shown in the April 21 *(b)* column of Fig. 6. Points of maximum brightness of two shells used in the derivation of the dust outflow velocity are indicated on the profiles by squares and diamonds. The brightness scale of the profiles is relative and arbitrary. The ordinate gives the radius in pixels from the photo-centre of the image along the radial profile. Selected profiles are labelled with the PA in which they were extracted. The PA of the sun for this observation was 243.1° relative to the nucleus

distance in question, the radial component of motion was calculated to $\dot{r} \sim 0.5 \pm 0.1$ km s^{-1}.

Assuming (on the basis of the regular coma spiral pattern) that the activity of the nucleus was periodic and showed similar outflow behaviour at each revolution during the period of observation, a given shell on a given night will be located two shell positions further from the nucleus the nest night. This is due to a time lapse between observations of nearly 24 h ($\sim 2P$). From shell positions on April 23, 24 and 25 images a least-squares straight line fit to the radius data points gives a mean projected outflow velocity of $\dot{r} = 0.41 \pm 0.02$ km s^{-1} over a range $r = 5\,000 - 45\,000$ km. The largest velocities measured from the width of the shells are $\dot{r}_{\max} = 0.55$ km s^{-1}.

7. Coma morphology

The emission pattern of the coma at radii $r < 80\,000$ km was highly heterogeneous with respect to r and θ on all dates. In the general solar direction, a system of shells at regularly spaced radii was visible. Five shells were seen by temporal derivative processing, each separated by $\Delta r \sim 20\,000$ km, and spiralling towards the photo-centre with decreasing radii in the direction of the evening terminator. The relative intensities of the photo-centre and the brightest regions of the three innermost shells were 1.00, 0.24, 0.07 and 0.04 on $\lambda\,830$ nm images obtained on April 24, subjected to basic reduction only.

An (r, θ)-coordinate system with origin at the photo-centre and the sub-solar direction of the respective image was introduced to facilitate interpretation of coma features. Features following (i.e. having smaller PA values), in the sense of rotation, the sub-solar direction have $\theta \in [-180, 0]$. A point on a hypothetical spherical nucleus with axis of rotation perpendicular to radius vector would be located at the morning terminator when $\theta = -90°$. Features preceding the sub-solar direction are characterised by $\theta \in [0, 180]$. A point at the evening terminator would have $\theta = 90°$.

On sharp images, the shell system was consisting of two superposed components, having similar mean radii, curvatures and intensities, and lagging each other by $\Delta\theta \sim 55°$. This effect was visible out to the third shell at $r \sim 47\,000$ km on April 24. The two-system shell morphology was not apparent in the outermost shells. The shells are characterised by sharp outer boundaries and more diffuse inner boundaries.

The sharpest and highest quality (in terms of S/N) images were obtained April 21 and 24. Unsharp masking, azimuthal renormalisation and rotational gradient processing effectively revealed low-contrast detail in the near-nucleus coma on images from these dates (Fig. 6). The effect of these processing methods is to remove the diffuse underlying coma emission from the image, thereby increasing the relative brightness of small-scale details.

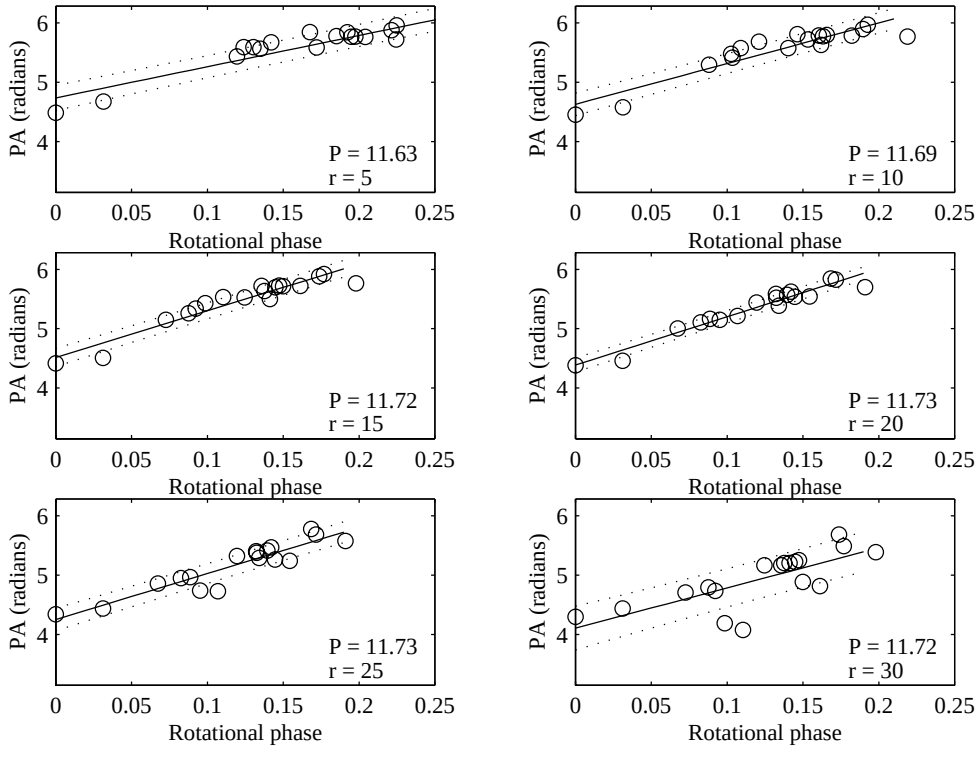

Fig. 5. Least-squares linear fits (solid lines) of the position angle and the rotational phase of fitted ($r_{\max}$, θ)-data, shown for six radii within the radius interval where isophote elongations were measured on the images. The rotational phase is defined as the fraction of the full rotation period P elapsed since the first image obtained on April 21. Best-fit rotation periods P and corresponding radii (r, in pixels) are given in the lower right-hand corner of each panel. Extrapolation of the $P(r)$ curve thus obtained to zero radius gives the nucleus rotation period of $11\overset{\text{h}}{.}46 \pm 0\overset{\text{h}}{.}25$. The dotted lines define a 50% error confidence interval of the fit

The first two methods produce output images with unaltered feature locations with respect to the input image. Characteristics of coma features are measurable with respect to location for unsharp masking and to location and size for azimuthal renormalisation, but not to relative intensity. Diffuse and large-scale features are well detected with azimuthal renormalisation and rotational gradient techniques, which are well removed by unsharp masking. Rotational gradient processing enhances regions of intensity gradients and may therefore be used to detect the presence of small-scale intensity variations, given that the angle of rotation of the subtracted image component is kept small. As most of the flux of the resulting image is removed, its S/N is low, requiring that the data intensity range of the input images covers a significant portion of the dynamic range of the CCD chip.

The effect of the convolution with the seeing disk effective during the exposure is well seen in Fig. 6, where the general features of the April 21 and 24 images are still detectable at the poor seeing conditions of April 25, but more diffuse and with lower S/N. For absolute characterisation of features in the following morphological description, measurements were made on images subject of basic reduction only, to assure a linear relative intensity scale.

7.1. April 21

April 21 images show an inner shell forming near the nucleus on the sub-solar hemisphere. It consists of two curved components, "subshells", at different radii, where the inner subshell is directly connected to the photo-centre by dust outflow on the morning hemisphere. It is of homogeneous intensity out to a distance of $r \sim 5\,200$ km from the photo-centre, where the intensity abruptly decreases. The subshell disappears into the background noise at (r, θ) $\sim$ (8 500 km, $-31°$).

The outer subshell at $r = 4\,500 - 12\,000$ km has a very irregular intensity and stretches to the evening terminator. It disappears into the background on the morning hemisphere at (r, θ) $\sim$ (12 000, $-12°$).

There is further a very faint and small jet-like feature visible on the anti-solar hemisphere, apparent as a narrow coma elongation passing through the point (r, θ) $\sim$ (2 000, $-130°$).

The second shell has a mean radius of 25 000 – 30 000 km and is more diffuse than the inferior shell with a similar general structure. The shell has two superposed components. The preceding one starts at a radius just outside of the inner shell spiral on the evening hemisphere at

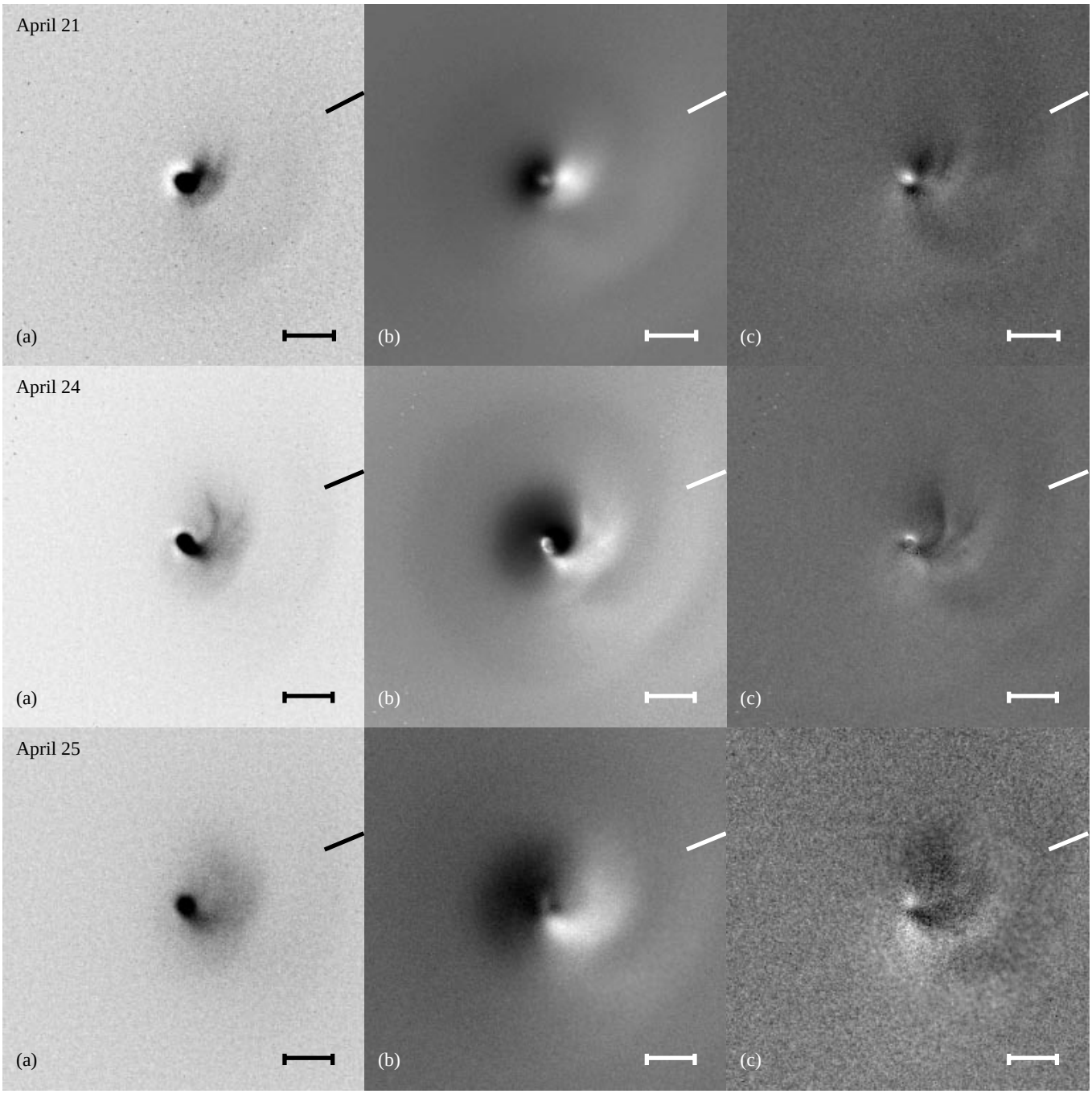

Fig. 6. Processed images of the near-nucleus region of Hale-Bopp on April 21 (21:24.6 UT), 24 (20:45.5 UT) and 25 (20:42.9 UT). In the leftmost **a)** frames, unsharp masking processing is shown, emphasising the innermost filament and shell structure. Amplification factors in the range $A = 1.0 - 1.3$ and high-pass filters of $n = 13$ were used. The middle column **b)** display azimuthal renormalisation processing and the rightmost column **c)** rotational gradient processing with $\Delta\theta = 10^{\circ}$ in order to enhance morphology more distant from the photo-centre. A linear intensity grayscale map from black to white indicates increasing brightness for **b)** and **c)** frames, while the intensity scale is inverted in **a)** frames. Frames are oriented with celestial south up and west to the right. The slanted lines mark the direction of the projected radius vector, which in **c)** frames is relative to the unrotated image component. Scale bars are 10 000 km; the field size corresponds to 73 000 km at the distance of the comet

$\theta \sim 100°$ as a wide diffuse arc emanating from the inner coma. It is curved towards the following hemisphere and connects to the second shell main dust trajectory. The following component of the shell is superposed on the preceding, emanating from a similar wide but slightly fainter diffuse arc discernible just outside the inner shell at $\theta \sim 20°$. The shell components have intensity maxima at $\theta \sim 75°$ and $\theta \sim 25°$, coinciding with the points of connection of the wide arcs to the main trajectory of the shell.

The third and fourth shells have too low S/N to show any associated diffuse arcs connecting them towards the nucleus, and are seen only as single-component shells with intensity maxima at $\theta \sim 38°$. Rotational gradient processing reveals only a steeper curvature of the third shell towards the photo-centre, at the assumed position of the aforementioned diffuse arc with origin at smaller radii.

7.2. April 23

April 23 images have low resolution due to bad seeing. They do not show small-scale features other than the major filament complex of the inner shell, at a time approximately four rotation periods later than those of April 21.

7.3. April 24

Morphology of the inner shell on April 24 is even more complex than on April 21, due to very stable seeing.

A major very bright and wide jet-like feature on the dayside at $\theta = 20°$ near the photo-centre dominates the flux of the inner shell. It starts curving at $r \sim 3\,000$ km. There is a rather sharp decrease in intensity at the outer boundary at $r = 15\,000 - 18\,000$ km as it separates into three filaments. The very bright and narrow filament on the following side of the major jet-like feature is visible on the morning hemisphere and reaches sky intensity at $(r, \theta) = (12\,000, -45°)$. It shows an extended intensity maximum at $(r, \theta) = (8\,900, -15°)$. Following this filament is a diffuse isolated patch at $(r, \theta) = (4\,300, -20°)$.

Two fainter, more diffuse filaments precede the inner filament at larger radii and have endpoints at $(r, \theta) = (14\,000, 0°)$ and $(r, \theta) = (12\,500, 25°)$ at the outer boundary of the first shell. At $(r, \theta) = (7\,500, 70°)$ there is an enhancement in intensity, relating to a region of locally higher dust opacity or the end of another filament. This point is located on the extreme preceding edge of the major jet-like feature.

A small jet-like feature is visible on the anti-solar hemisphere at $\Delta\theta = -105°$ close to the photo-centre. It starts curving in the following direction at $r \sim 2\,500$ km and forms a spiralling filament stretching into the sub-solar hemisphere, apparently joining the inner shell.

The second shell from the photo-centre shows a double aspect as on April 21, with two main superposed components separated by $\Delta r = 6\,000$ km, diffusing in the following direction.

The third and fourth shells show only a single aspect with intensity maxima at $\Delta\theta \sim 30°$. As on April 21, the third shell is curved towards the photo-centre at the apparent location of the wide arc connecting to the inner coma. The feature is most apparent on images of long exposure times, processed with the rotational gradient method.

7.4. April 25

April 25 images have lower resolution and S/N ratio than those of April 24 but still show signs of similar activity. Only the first and second shells are prominent.

The morphology of the coma was thus very complex during the period of observation, with small-scale patches apparent both within and separated from the filaments. On April 21 images, unsharp masking processing (Fig. 6) reveals that the outer subshell of the inner shell was outlined by five diffuse light patches with sizes of $\sim 1\,000 - 2\,000$ km. From the mean dust outflow velocity and distance to the photo-centre, this matter was emitted from the nucleus at least $\sim$8 h before the image was obtained. If the size of the patches is directly correlated with increased intermittent activity of the nucleus emission region and not due to gas and dust grain interaction processes within the coma, these periods had durations of $\sim$1 h or less. Similar patches were apparent on April 24. The contrast of the brightest of these patches is $\sim$1% relative to the brightness of the neighbouring filament trajectory, as measured on images from April 21 and 24 subjected to basic reduction only.

The inner and bright filaments apparent in the inner shell of April 24 contain each 0.09 ± 0.01 of the flux within radii of $4\,000 - 14\,000$ km, corresponding to the area of first shell outside of the point where the filaments are separable. Thus, the filaments within the otherwise diffuse emission of the first shell visible on April 24 carry a non-insignificant amount of the projected dust column density, and may carry a significant part of the total dust emitted. It seems clear from these figures also that a major part of the dust flux is attributable to structures with spatial sizes below the resolution limit of the present observations.

Regarding the global shape of the shell spiral pattern, analysis of images from April 24 subjected to a $\Delta\theta = 10°$ rotational derivative processing (Fig. 6) shows that the steepness of the spiral, $\Delta r/\Delta\theta$, is dependent on θ. The geometric centre of the pattern is close to the photo-centre position and the magnitude of $\Delta r/\Delta\theta$ is small, indicating that the angle of the rotational axis to the line of sight ψ is not very large. An estimation of the value of ψ requires a more rigorous treatment of the data.

8. Discussion and conclusions

We present high resolution images of the dust continuum optical emission in the coma of comet Hale-Bopp on April 21–25 1997, within a radius of 72 000 km of the photocentre. On processed images, coma detail is visible at characteristic sizes and nuclear distances of ∼2 000 km or less. The dust pattern has been described in terms of morphology and relative intensity, and is very complex. It is shown that the filaments visible in the inner shell during this period do not constitute the major part of the flux from the shell, which is rather dominated by the extended diffuse emission. From the cyclic appearance of features, a nucleus rotation period of $P = 11\overset{\text{h}}{.}46 \pm 0\overset{\text{h}}{.}25$ and a mean dust outflow terminal velocity of $\dot{r} = 0.41 \pm 0.02$ km s^{-1} has been determined. The north pole of the nucleus was directed towards the Earth, as given by the sense of rotation of the dust features.

It has been shown (e.g., by Kitamura 1986, 1987, 1990; Crifo et al. 1997a, 1997b, 1990) that the correlation between visible coma features and the location of the emitting nucleus source or sources is not trivial, especially not in the case of an active comet. Hydrodynamic modelling of gas and dust outflow reveal that an observed filament in the coma may be produced from the gas-dynamic interaction of emission activity from more than one source, and that higher-order daughter filaments are produced at larger radii by dust and gas interaction closer to the nucleus.

The fact that the outflow activity of a compositionally homogeneous aspherical nucleus will produce shock fronts and filaments similar to that of a compositionally inhomogeneous spherical nucleus, indicates that coma structure may not give any intuitive information on the location of the emitting source regions. Interpretation of the three dimensional structure of the Hale-Bopp inner coma from images such as those presented here in terms of nucleus activity is further complicated by several factors, e.g., the integration of the dust brightness flux along the line of sight, the probable diurnal cycles of the sources, the probably complex shapes and rotational states of the nucleus or nuclei, and the unknown dust size and velocity distributions. We have an estimate on the size of the dust grains from Williams et al. (1997) who found the optically important grains dominating the visual scattering and near-infrared emission from the coma to have an average radius of $\leq 0.4\,\mu$m, based on infrared spectrophotometric observations.

The value of the rotational period agrees well with the determinations of earlier works. A longer period of observations would undoubtedly have improved the error bars of the figure. A rotation period of $11\overset{\text{h}}{.}47 \pm 0\overset{\text{h}}{.}05$ was determined from from images obtained Jan. 12-Feb. 10 1997 (Lecacheux et al. 1997), oscillating between $11\overset{\text{h}}{.}20 \pm 0\overset{\text{h}}{.}10$ and $11\overset{\text{h}}{.}65 \pm 0\overset{\text{h}}{.}10$ (Jorda et al. 1997). A period of $11\overset{\text{h}}{.}3$ was obtained from images taken at perihelion (Lisse et al. 1997) and from mid-infrared images (Sarmecanic et al. 1997a, 1997b), $11\overset{\text{h}}{.}33 \pm 0\overset{\text{h}}{.}05$ from motion of dust arcs (Farnham et al. 1998), and $11\overset{\text{h}}{.}34 \pm 0\overset{\text{h}}{.}02$ by Licandro et al. (1998). Long daylight observation sequences by the European Hale-Bopp team in April 1997[2] indicates a period of $11\overset{\text{h}}{.}20$.

A possible longer period of emission activity of ∼20 days has been reported (e.g., Sekanina 1996; Jorda et al. 1997a; Kidger 1998), which has been attributed to precession of the nucleus. During the five day timeframe of the present observations, deviation from a pure spin rotational state may, in addition to errors of measurement, contribute to the error in the value of the obtained rotation period, which is based on a "pure spin" assumption. However, a very complex state of rotation of the nucleus is contradicted by the work of Licandro et al. (1998) based on observations obtained during a time period similar to the length of the suggested precession period.

The direction of the axis of rotation of the nucleus has been determined from Monte-Carlo image simulations and the application of different emission models (Sekanina & Boehnhardt 1997, 1998; Sekanina 1998), the results of which give somewhat contradictory results. It is possible, from results of gas-hydrodynamic modelling, that the rotational state of the nucleus may be very difficult to extract from imaging of coma features as filaments may be created by second-order interaction effects far from the source of emission, and thus not trace the movement of the nucleus.

The mean terminal expansion velocity of the dust shells determined here is slightly higher than published values of ∼0.3 km s^{-1} from CCD imaging in Jan.-Feb. 1997 (Lecacheux et al. 1997), and $0.30 - 0.35$ km s^{-1} on Feb. 22, 1997 by Jorda et al.[3] From near-infrared observations, a velocity of the order of $0.35 - 0.45$ km s^{-1} were determined by Mannucci & Tozzi (1997) from observations on Feb. 3 and 10, 1997. The determination of outflow velocity is uncertain partly due to the observing circumstances. With a longer observing run and higher S/N data, a greater number of shells would have been measurable over a longer time span, improving the estimate. Further, this velocity estimate integrated over dust grain size and line-of-sight effects is a mean value in a broad sense.

The complex structure of the filaments may be a result of variable activity of the active region(s) on the nucleus, or due to interaction of expanding outflowing dust volumes. We have limited ourselves to the morphological description of visible coma features, and hope that

[2] At the time of writing, this information may be obtained from the Comet Hale-Bopp European Team Homepage at http://www.iac.es/comet/hbet.html

[3] At the time of writing, this information may be obtained from the Pic du Midi Hale-Bopp Homepage at http://www.bdl.fr/s2p/comete/halebopp/halebopp.html

numerical simulation experiments and hydrodynamic modelling of the gas and dust interaction of the inner coma will benefit from detailed high resolution images such as those obtained by the SVST.

Acknowledgements. This work was made possible by a grant from the Anna and Allan Löfberg Foundation. Professor Göran Scharmer (Stockholm Observatory) is much thanked for providing observing time at the SVST. The observations would not have been possible without assistance from the SVST staff Göran Hosinsky and Rolf Kever. The comments of the anonymous referee were valuable in improving the paper.

References

Blumberg R.E., Boksenberg A., 1996, The Astronomical Almanac 1997, Nautical Almanac Office, United States Naval Observatory
Crifo J.F., Itkin A.L., Rodionov A.V., 1995, Icarus 116, 77
Crifo J.F., Rodionov A.V., 1997a, Icarus 129, 72
Crifo J.F., Rodionov A.V., 1997b, Icarus 127, 319
ESO, 1996, Munich Image Data Analysis System, European Southern Observatory, 96NOV edition
Farnham T., Schleicher D., Blount E., Ford E., 1998, Earth, Moon, Planets (submitted)
Gonzalez R.C., Woods R.E., 1992, Digital Image Processing. Addison-Wesley Publishing Company
James P., Clancy T., Lee S., NASA, 1997, Mars North Polar Cap, PRC97-15b, ST ScI OPO
Jorda L., Lecacheux J., Colas F., 1997, Comet C/1995 O1 (Hale-Bopp), IAU Circular 6583
Keller H.U., Knollenberg J., Markiewics W.J., 1994, Collimation of cometary dust jets and filaments, Planet. Spacce Sci. 42, 367
Kidger M., 1998, Earth, Moon, Planets (submitted)
Kitamura Y., 1986, Icarus 66, 241
Kitamura Y., 1987, Icarus 72, 555
Kitamura Y., 1987, Icarus 86, 455
Kömle N.I., Ip W.-H., 1987, A&A 187, 405
Larson S.M., Slaughter C.D., 1992, in: Harris A.W. and Bowell E. (eds.), Asteroids, Comets, Meteors 1991. Lunar and Planetary Institute. Houston, pp. 337–343
Lecacheux J., Jorda L., Colas F., 1997, Comet C/1995 O1 (Hale-Bopp), IAU Circular 6560
Licandro J., Bellot Rubio L.R., Boehnhardt H., et al., 1997, Bull. Am. Astron. Soc. 29, 3
Licandro J., Bellot Rubio L.R., Boehnhardt H., et al., 1998, AJ 501, L221
Lindgren M., 1995, Ph.D. thesis, Uppsala University
Lisse C.M., Fernandez Y.R., A'Hearn M.F., et al., 1997, Bull. Am. Astron. Soc. 29, 3
Mannucci F., Tozzi G.P., 1997, Comet C/1995 O1 (Hale-Bopp), IAU Circular 6575
Marsden B.G., 1997, C/1995 O1 (Hale-Bopp), Minor Planet Circular 30738, Minor Planet Center, Smithsonian Astrophysical Observatory
Orton G., Ortiz J.L., Baines K., et al., 1996, Sci 272, 839
Samarasinha N.H., Mueller B.E.A., Belton M.J.S., 1998, Earth, Moon, Planets (submitted)
Sarmecanic J., Osip D.J., Fomenkova M., Jones B., 1997, Comet C/1995 O1 (Hale-Bopp), IAU Circular 6600
Sarmecanic J.R., Osip D.J., Lederer S.M., Fomenkova M.N., Jones B., 1997, Bull. Am. Astron. Soc. 29, 3
Scharmer G.B., Brown D.S., Petterson L., Rehn J., 1985, Appl. Opt. 24, 16
Sekanina Z., 1987, in: Rolfe E. and Battrick J. (eds.), Symposium on the Diversity and Similarity of Comets, ESA SP-278, pp. 315–322
Sekanina Z., 1996, A&A 314, 957
Sekanina Z., 1998, ApJL 494, L121
Sekanina Z., Boehnhardt H., 1997, Comet C/1995 O1 (Hale-Bopp), IAU Circular 6542
Sekanina Z., Boehnhardt H., 1998, Earth, Moon, Planets (submitted)
Sekanina Z., Larson S.M., 1986, AJ 92, 462
Warell J., 1996, Earth, Moon, Planets 74, 93
Williams D.M., Mason C.G., Gehrz R.D., Jones T.J., et al., 1997, ApJL 489, L91
Yeomans D.K., 1997, JPL Reference Orbit 59